Supplementary Information

Cathode chemomechanics controls Li metal solid-state battery performance under low stack pressures

Saeed Moradi[1,2,3], Beniamin Zahiri[1,2,*], Paul V. Braun[1,2,3,4,5*]

[1]Department of Materials Science and Engineering, University of Illinois Urbana-Champaign, Urbana, IL 61801, USA

[2]Materials Research Laboratory, University of Illinois Urbana-Champaign, Urbana, IL 61801, USA

[3]Department of Chemical and Biomolecular Engineering, University of Illinois Urbana-Champaign, Urbana, IL, 61801, USA

[4]Department of Chemistry, University of Illinois Urbana-Champaign, Urbana, IL 61801, USA

[5]Beckman Institute for Advanced Science and Technology, University of Illinois Urbana-Champaign, Urbana, IL 61801, USA

*Corresponding authors: pbraun@illinois.edu, bzahiri@illinois.edu

S1. 003-LCO and 110-LCO Microstructure

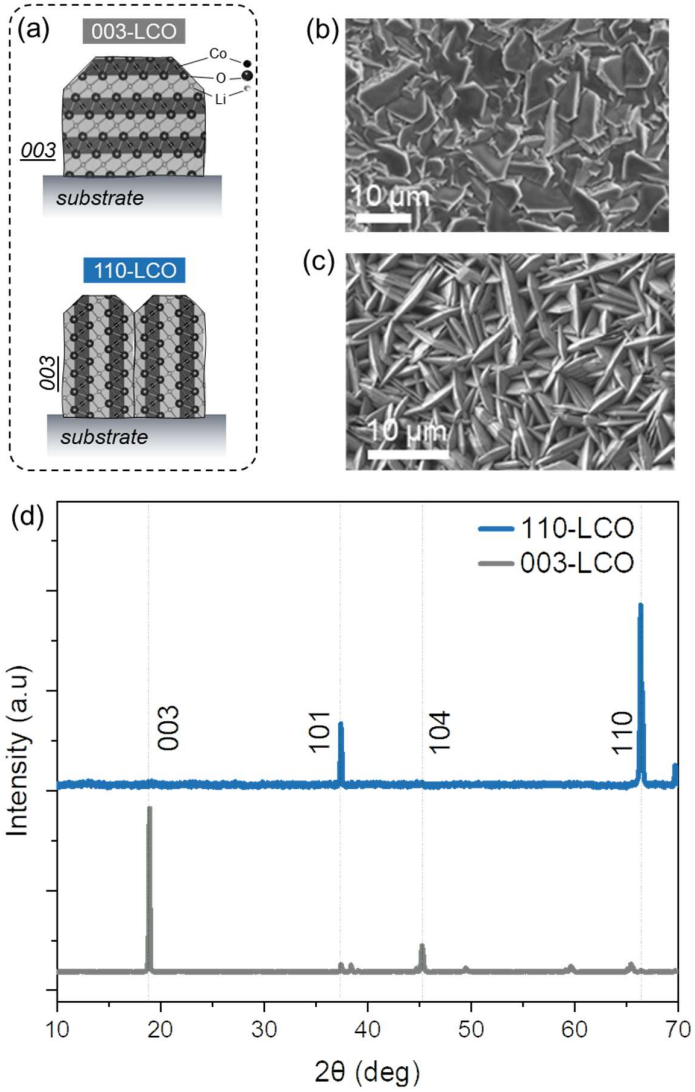

Figure S1 | Crystallographic and microstructural characterization of textured LCO cathodes. (a) Schematic representation of 003-LCO and 110-LCO crystallographic structures, illustrating the orientation of crystal planes relative to the substrate, where 003-LCO has the c-axis parallel to the substrate and 110-LCO has ab-planes parallel to the substrate. This highlights the anisotropic nature of LCO chemomechanics during lithium deintercalation. (b) Top-view SEM image of 003-LCO, showing the surface morphology with densely packed grains and minimal porosity. (c) Top-view SEM image of 110-LCO, displaying a distinct morphology with elongated features aligned along the ab-plane, confirming the crystallographic texture. (d) X-ray diffraction patterns of 003-LCO and 110-LCO, demonstrating dominant (003) reflections in 003-LCO and (110) reflections in 110-LCO, verifying the preferred orientations and phase purity.

S2. XRD texture analysis of *ab*-LCOs

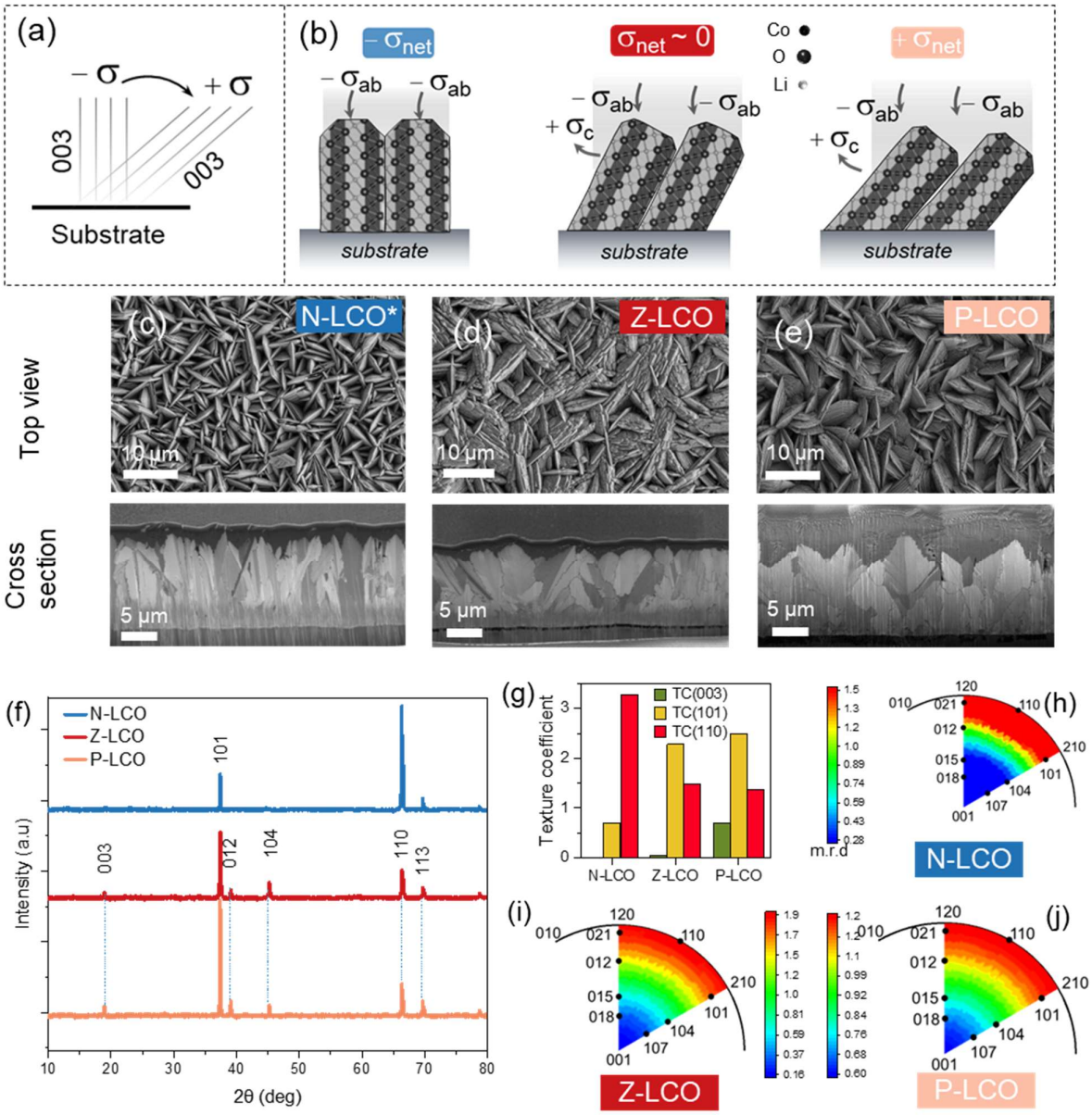

Figure S2 | Crystallographic texture oriented LCO positive electrodes. (a) Schematic of the relation between 003 plane orientation and the pressure generated by LCO positive electrode chemomechanics during delithiation (charging). (b) Schematic representation of three positive electrode structures (*ab*-LCOs) with similar morphology but altered texture components resulting in three distinct chemomechanical response. P, Z and N refer to positive, zero, and negative stress generation during delithiation. (c-e) Top and cross-sectional SEM micrographs of the three positive electrode structures confirming similar morphological features at the micro-scale. (f) XRD of N-LCO, Z-LCO, and P-LCO showing the peak intensity variation in major LCO reflections. (g) Calculated texture coefficients of 003, 101 and 110 reflections. 110 component is the largest in N-LCO, 101 component is larger in Z-LCO and P-LCO, and 003 component is significant in P-LCO. (h-j) Calculated inverse pole figures in the direction normal to the substrate showing the preferred orientation is 110 with a dominant {110}<001> type texture for all these LCOs. *N-LCO is same as the 110-LCO shown in Fig. 1. Multiples of random distribution (m.r.d) indicates how much the orientation of crystallites deviates from a random orientation. The layered structure of $LiCoO_2$ was illustrated with VESTA software.[1]

Table S1: Comparison of peak (areal) intensity ratio and texture coefficient (TC) of major planes for powder and electrodeposited LCOs vs. LCO standard (PDF# 51182).

	$I_{003/101}$	$I_{003/104}$	$I_{003/110}$	$TC_{(003)}$	$TC_{(101)}$	$TC_{(104)}$	$TC_{(110)}$
LCO_{std}	5.24	1.53	5.89				
Powder LCO	5.06	3.13	9.72	1.28	1.32	0.63	0.77
P-LCO	0.14	1.26	0.3	0.7	2.49	0.08	1.36
Z-LCO	0.12	0.45	0.21	0.05	2.28	0.18	1.48
N-LCO	0.03	0.73	0.01	0.01	0.7	0.01	3.28

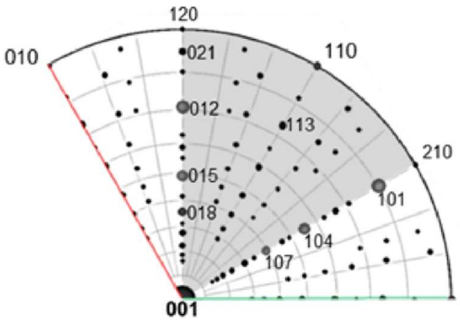

Figure S3 | Reference stereographic projection of LCO crystal. [001] zone axis produced with WinWulff software (@JCrystalSoft).

S3. Chemomechanics of *ab*-LCOs

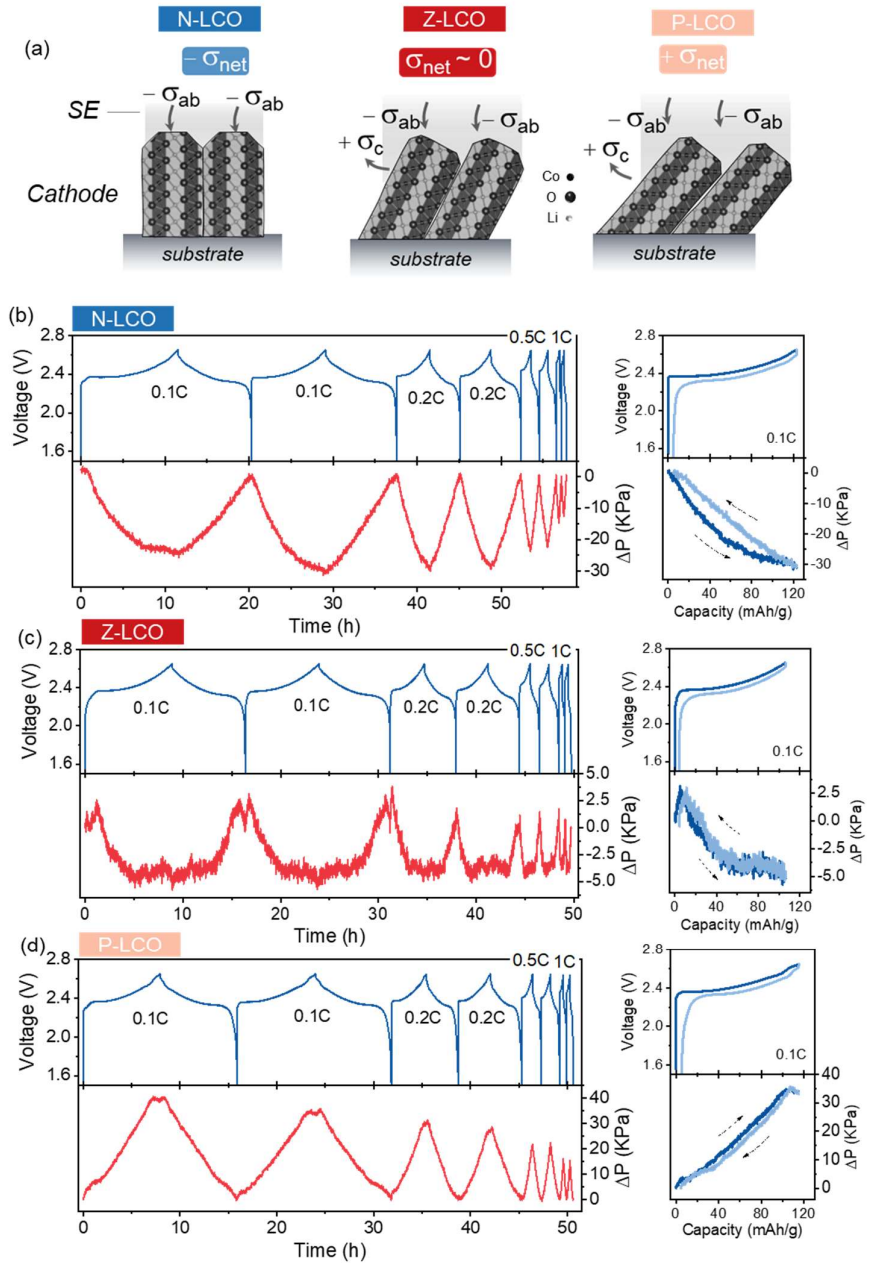

Figure S4 | Chemomechanical responses of textured ab-LCO positive electrodes at different cycling rates. (a) Schematic representation of three *ab*-LCO positive electrode structures with similar morphology and altered texture components resulting in three distinct chemomechanical response. P, Z and N refer to positive, zero, and negative stress response. (b) N-LCO (c) Z-LCO and (d) P-LCO voltage and pressure at cycling rates of 0.1C (0.12 mA/cm^2), 0.2C (0.24 mA/cm^2), 0.5C (0.6 mA/cm^2) and 1C (1.2 mA/cm^2) in cell configuration of LTO|LYC|LIC|LCO at 26°C and 60 MPa. Positive electrodes loading are 1.2 mAh/cm^2. The right panels show reversible pressure response in the second 0.1C (0.12 mA/cm^2) cycle.

S4. XRD analysis of *ab*-LCOs peak position vs. charge

XRD analysis of three LCOs before and after the first charge cycle shows similar state-of-charge (SOCs) is achieved in all three samples based on the relative peak position shift in major 003, 101, and 110 reflections.

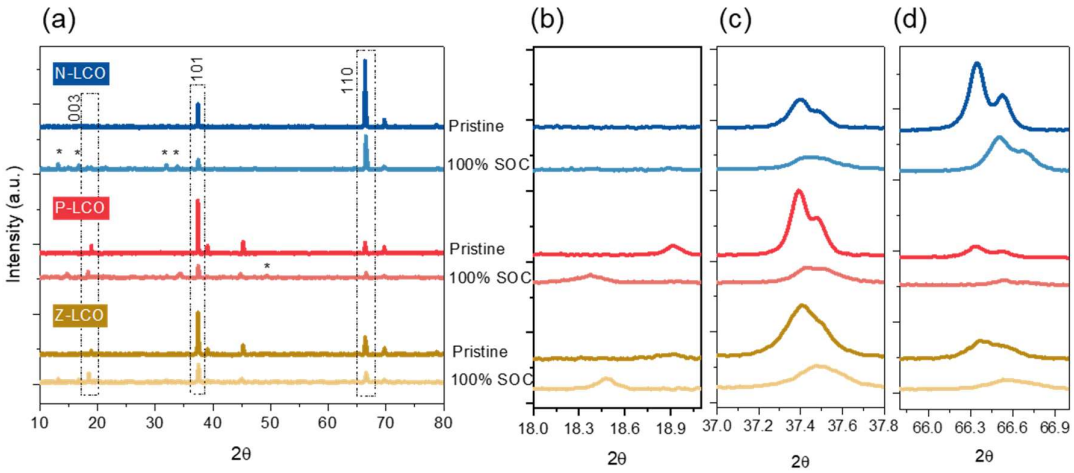

Fig. S5 | XRD analysis of textured LCO positive electrodes at pristine and fully charged states. (a) XRD of N-LCO, P-LCO, and Z-LCO at before charging (pristine state) and full state-of-charge (SOC) (100% charged under 0.12 mA/cm^2 and 4.2Vcut-off-Areal loadings 1.2 mAh/cm^2- 60 MPa and 26°C) and (b-d) XRD profiles near 003, 101, and 110, reflections.

S5. Chemomechanical response of composite positive electrodes

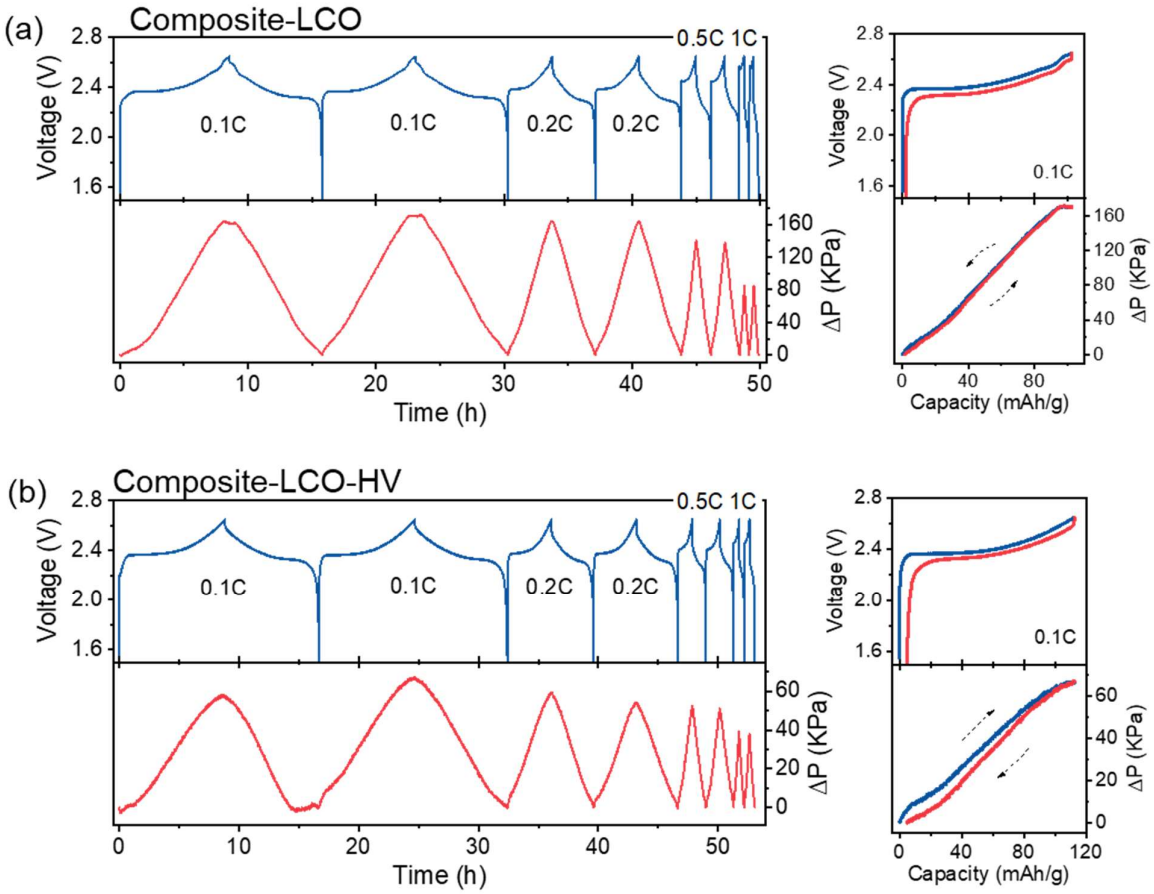

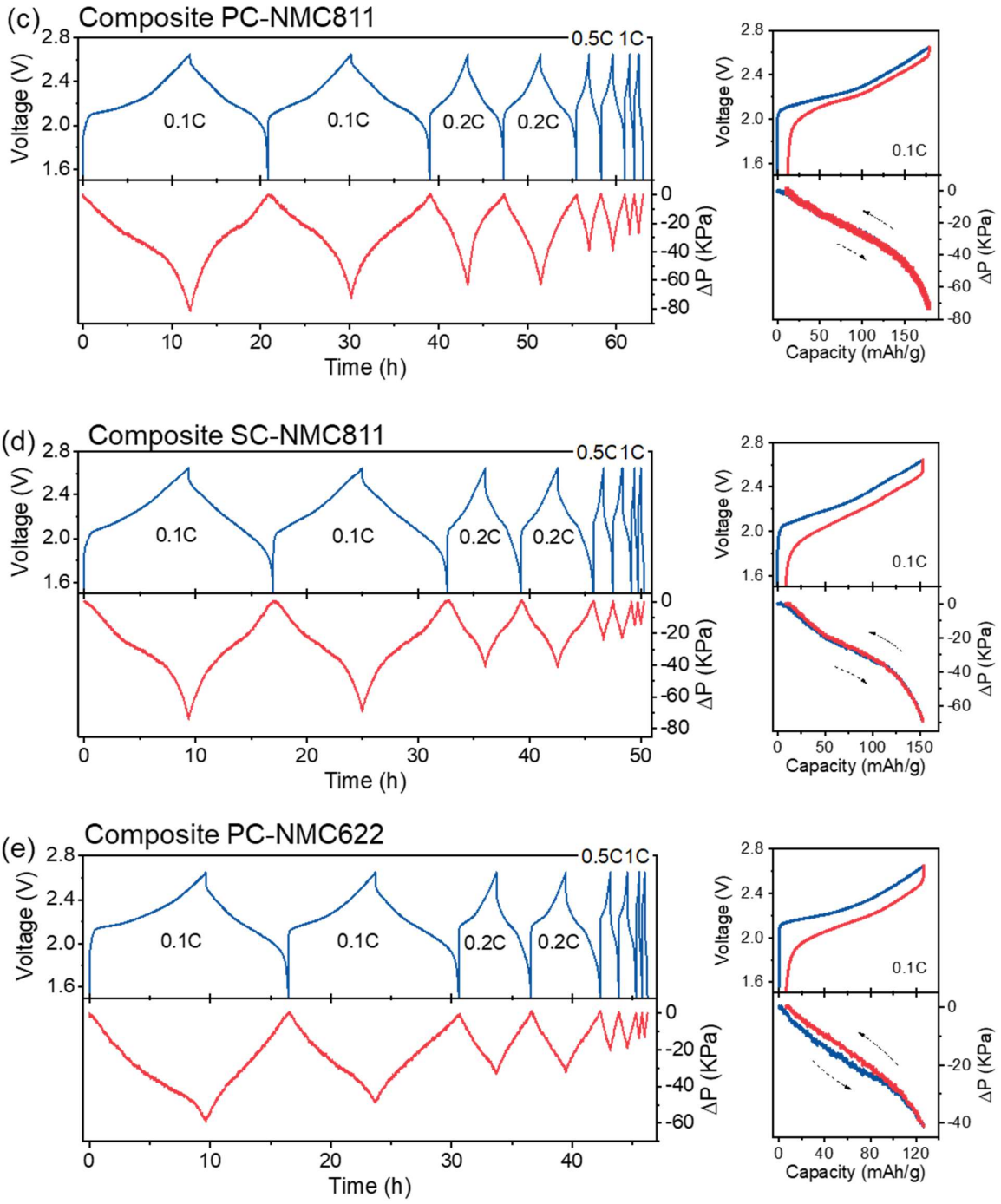

Figure S6 | Axial pressure responses of composite LCOs and NMC positive electrodes at different cycling rates. (a) Composite LCO, (b) high-voltage composite-LCO, (c) Composite PC-NMC811, (d) Composite SC-NMC811, (e) Composite PC-NMC622, at cycling rates of 0.1C (0.12 mA/cm^2), 0.2C (0.24 mA/cm^2), 0.5C (0.6 mA/cm^2) and 1C (1.2 mA/cm^2) in cell configuration of LTO|LYC|LIC|NMC at 26.6°C and 60 MPa. The right panels show reversible pressure response in the second 0.1C (0.12 mA/cm^2) cycle. Positive electrodes loading are 1.2 mAh/cm^2.

S6. Chemomechanics of cycling conditions and solid electrolyte decomposition

To understand the impact of cycling protocols, a few scenarios are presented. A typical charge protocol for both conventional and solid-state LIBs involves applying constant current followed by a constant voltage (CC-CV) hold. We evaluated the chemomechanical response of composite and dense positive electrodes during a voltage hold in Fig. S7. A distinct feature of the NMC positive electrode (Fig. S7 (a)) is continuous shrinkage upon holding, in line with expected delithiation induced steepening of volumetric changes based on diffraction data.[2,3] Conversely, LCO (Fig. S7 (b)) shows a flattening during the voltage hold which is also in line with the reversal in the direction of lattice volumetric change from overall expansion to contraction beyond half delithiation.[4,5] Similar behavior is also observed for dense LCO positive electrodes (P and N-LCO) as shown in Fig. S7 (c and d). The impact of cycling rate is shown in Fig. 3 (e and f). We observe that the slope of pressure evolution remains almost unchanged as charging rate increases from 0.1C to 1C, confirming that the major contributor to the stack pressure variation is degree of delithiation in lattice (that is state-of-charge). The role of SE decomposition is also inspected by controlling the voltage cutoff (beyond voltage stability of LIC, 4.2 V vs Li^+/Li). Fig. S7 (g) shows the chemomechanical response of LCO|LIC interface evaluated initially to 4.2 V vs Li and subsequently to 4.5 V vs Li^+/Li. As shown schematically in Fig. S8, the ab-plane dominant structure of N-LCO undergoes a slight expansion upon overcharging (> 4.2 V vs Li^+/Li) which translates into a reversal in decreasing trend in stack pressure beyond 4.2 V vs Li^+/Li. However, the observed further drop in stress suggests that the LIC decomposition results in volume shrinkage during high voltage events. Similar behavior has been observed for SE decomposition upon oxidation.[6,7]

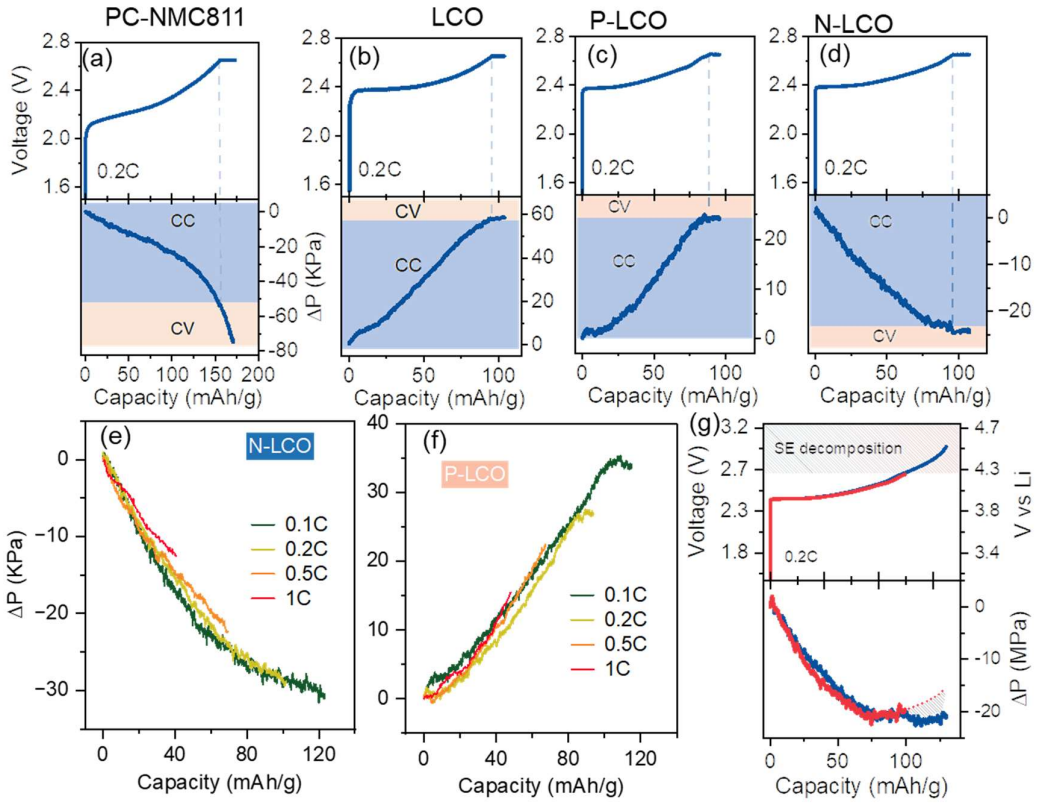

Figure S7 | Chemomechanical responses of LCO and NMC positive electrodes during CC-CV charging, rate-dependent cycling, and solid electrolyte decomposition. (a) PC-NMC811. (b) Composite LCO (c) P-LCO (d) N-LCO during constant current (CC) and constant voltage (CV) charge process. (e-f) The chemomechanical responses of N-LCO and P-LCO at 0.1C (0.12 mA/cm^2), 0.2C (0.24 mA/cm^2), 0.5C (0.6 mA/cm^2) and 1C (1.2

mA/cm^2) shows the dependency of stresses generated inside the battery to the degree of delithiation. (g) Effect of solid electrolyte decomposition at the voltages beyond LIC voltage stability region (>2.75 V vs LTO) on the chemomechanics of the cell. All of the cells are in the configuration of LTO||LYC|LIC|Positive electrode at 26°C and the stack pressure of 60 MPa, positive electrodes loading are equivalent of 1.2 mAh/cm^2.

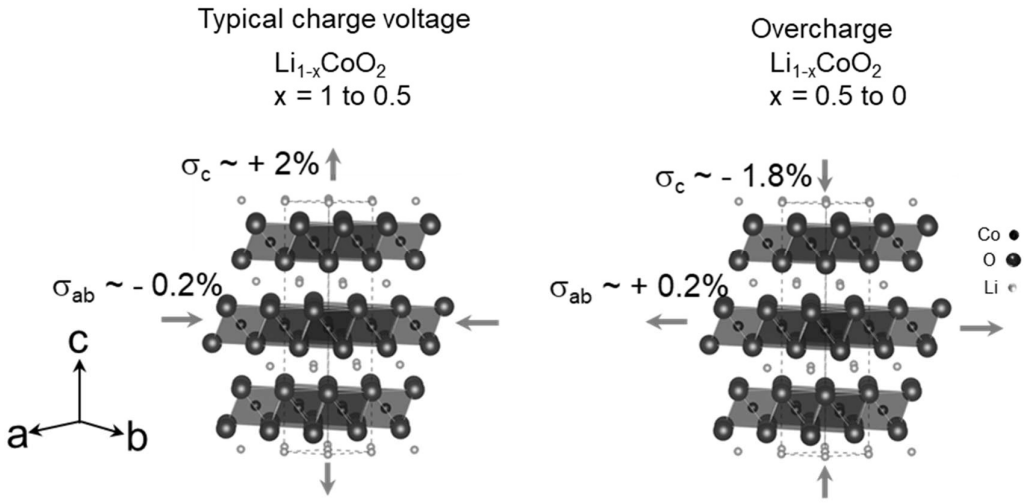

Figure S8 | Schematic representation of anisotropic volume changes of $Li_{1-x}CoO_2$ at typical delithiation range (x=1-0.50) and overcharged range (x < 0.5).

S7. Cycling of *ab*-LCOs against zero-strain anode

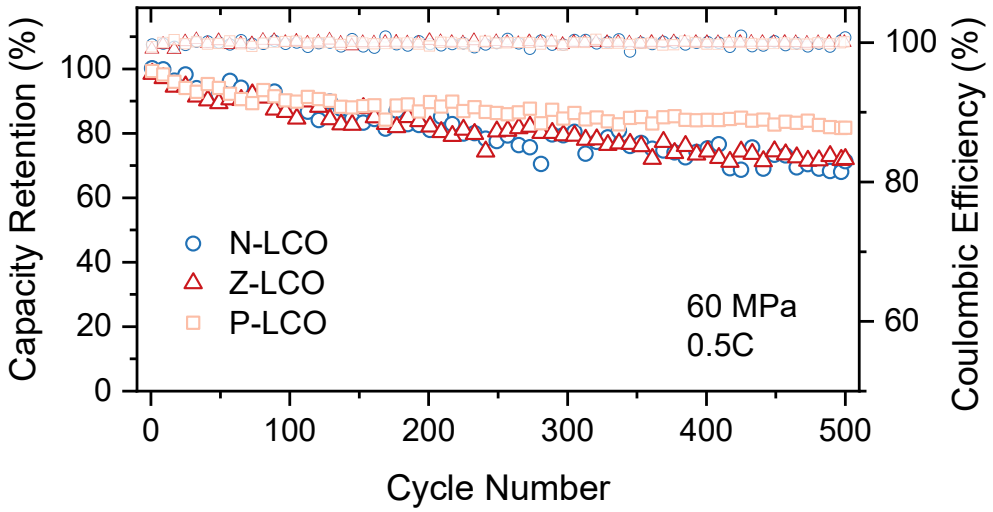

Figure S9 | Cycling performance of N-LCO, Z-LCO, and P-LCO positive electrodes vs LTO under high stack pressure. Cycling performance of N-LCO, Z-LCO, and P-LCO against zero-strain LTO anode with a cell configuration of LTO||LYC|LIC|Positive electrode at room temperature and 60 MPa. Positive electrodes loading are 1.2 mAh/cm^2. Capacity retentions for N-LCO, Z-LCO, and P-LCO are 70%, 75%, and 85%, respectively. Cycling data shown excludes the initial formation cycle. (0.5C=0.6 mA/cm^2)

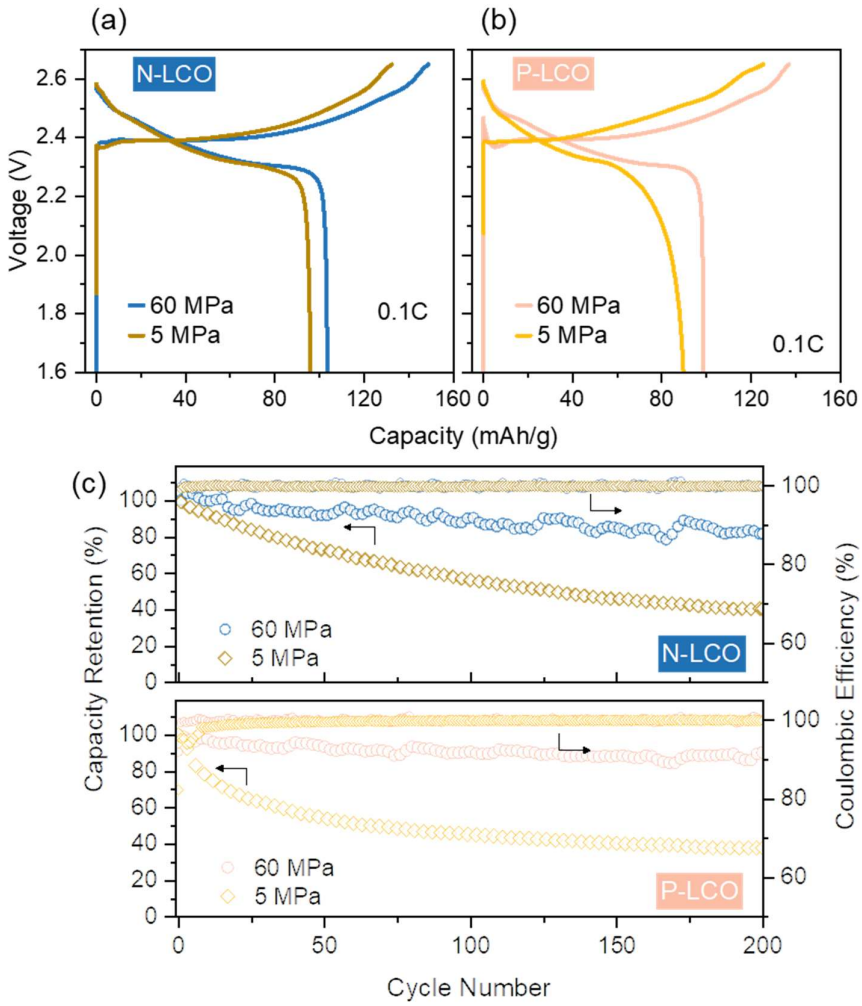

Figure S10 | Formation cycles and cycling performance of N-LCO and P-LCO positive electrodes at 5 MPa and 60 MPa stack pressures. Formation cycles for (a) N-LCO and (b) P-LCO at 60 MPa and 5 MPa at room temperature against zero-strain anode with a cell configuration of LTO|LYC|LIC|Positive electrode (c) Comparison of cycling performance of N-LCO and P-LCO at stack pressures of 60 MPa and 5 MPa at 0.5C (0.6 mA/cm^2) rate. Capacity retention for N-LCO at 60 MPa and 5 MPa is more than 80% and 40%, respectively. For P-LCO at 60 MPa and 5 MPa, capacity retention is approximately 95% and 40%. Positive electrodes loading are 1.2 mAh/cm^2. Cycling data shown excludes the initial formation cycle.

S8. Critical current density against Li metal anode

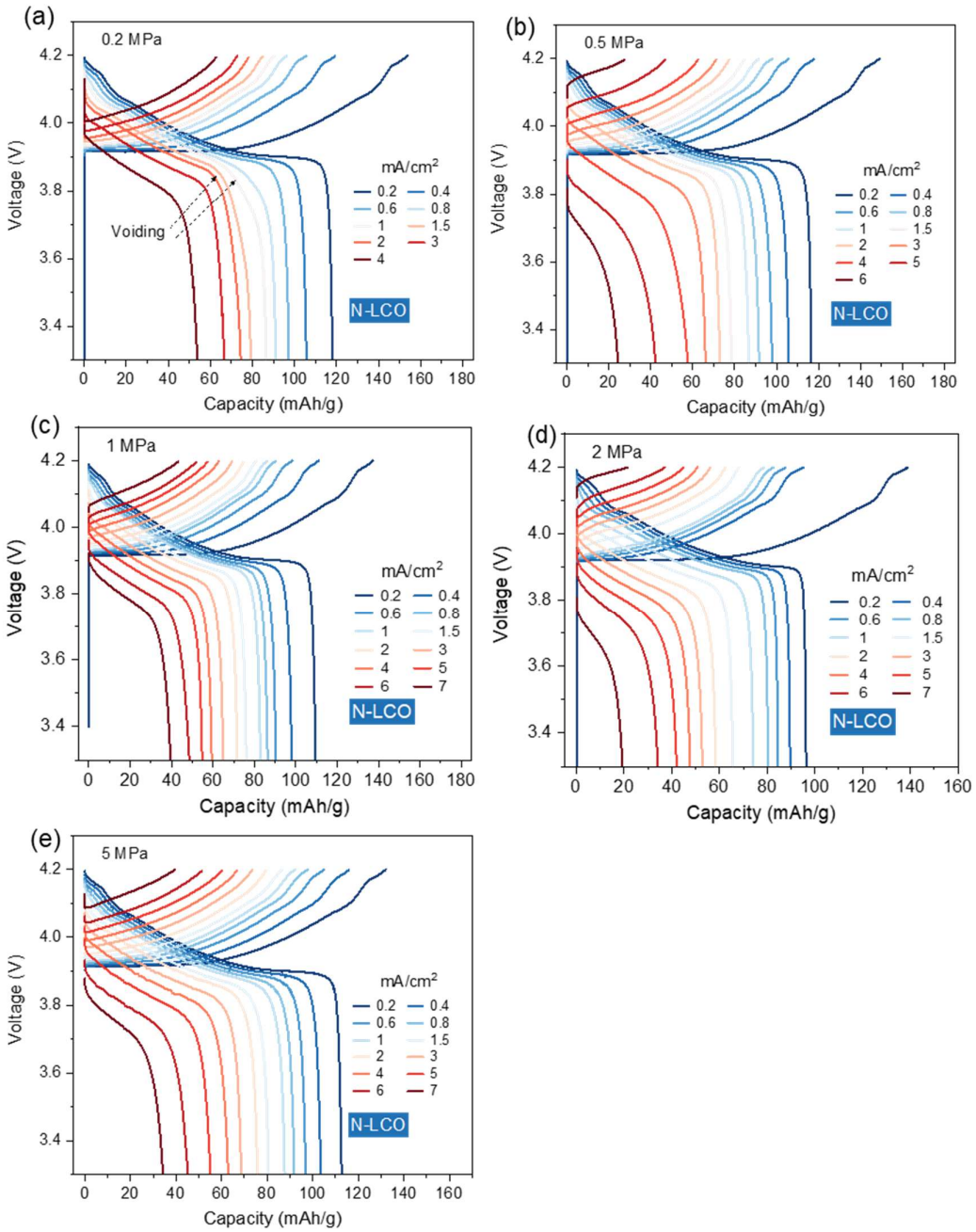

Figure S11 | Charge-discharge profiles of N-LCO positive electrodes at different stack pressures with stepwise increasing current density. (a - e) Charge-discharge profiles of N-LCO positive electrodes under stepwise increasing current density and 0.2 MPa, 0.5 MPa, 1 MPa, 2 MPa, and 5 MPa stack pressure with a cell configuration of Li|LPSC|LIC|Positive electrode. Voiding events during discharge resembling sudden slope change and voltage spikes are shown with arrows.

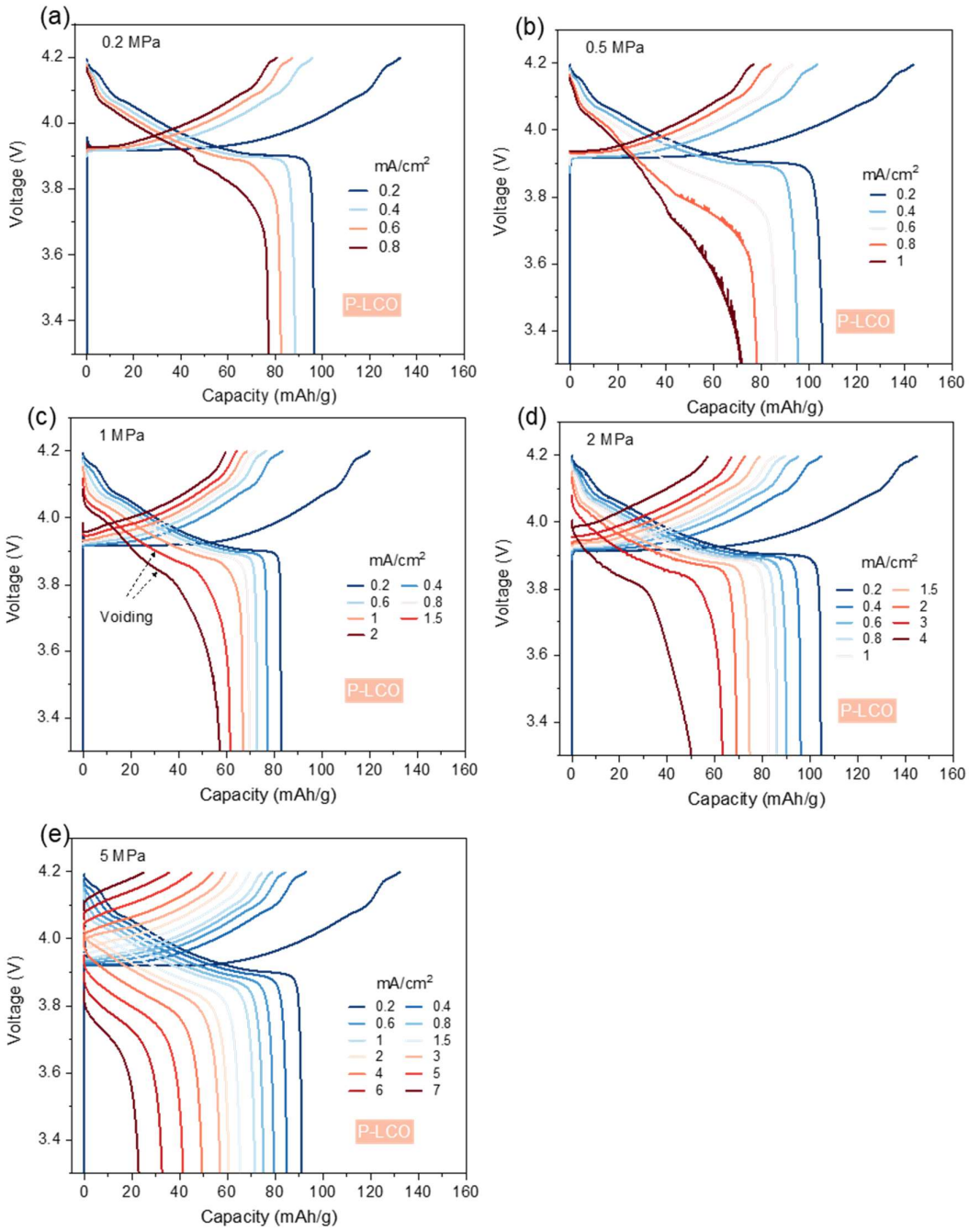

Figure S12 | Charge-discharge profiles of P-LCO positive electrodes at different stack pressures with stepwise increasing current density. (a - e) Charge-discharge profiles of P-LCO positive electrodes under stepwise increasing current density and 0.2 MPa, 0.5 MPa, 1 MPa, 2 MPa, and 5 MPa stack pressure with a cell configuration of Li|LPSC|LIC|Positive electrode. Voiding events during discharge resembling sudden slope change and voltage spikes are shown with arrows.

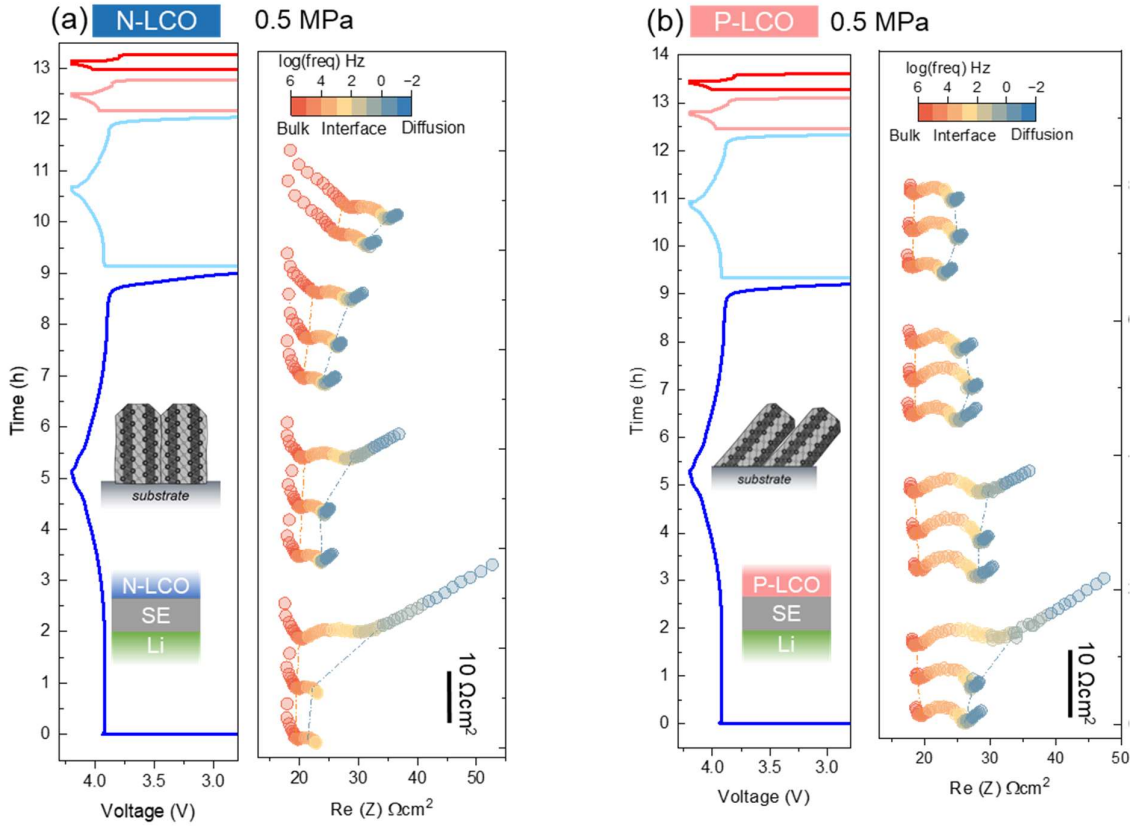

Figure S13 | Intra-cycle impedance of N-LCO and P-LCO positive electrodes at different cycling rates under low stack pressure. (a) Nyquist plots for the N-LCO cathode, showing intra-cycle impedance measurements during cycling at rates of 0.1C (0.12 mA/cm²), 0.2C (0.24 mA/cm²), 0.5C (0.6 mA/cm²), and 1C (1.2 mA/cm²) under 0.5 MPa stack pressure at room temperature. (b) Corresponding Nyquist plots for the P-LCO cathode under the same condition. For each cycle, the EIS data is collected after fully charged, partially discharged, and fully discharged states. Positive electrodes loading are 1.2 mAh/cm^2 with a cell configuration of Li|LPSC|LIC|Positive electrode EIS data points are colored based on their corresponding frequency as shown in the inset color map.

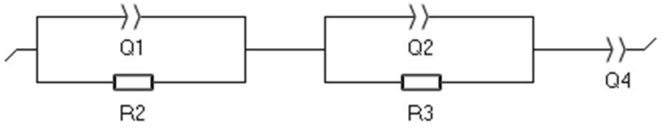

Figure S14 | EIS EC model used for EIS data fittings.

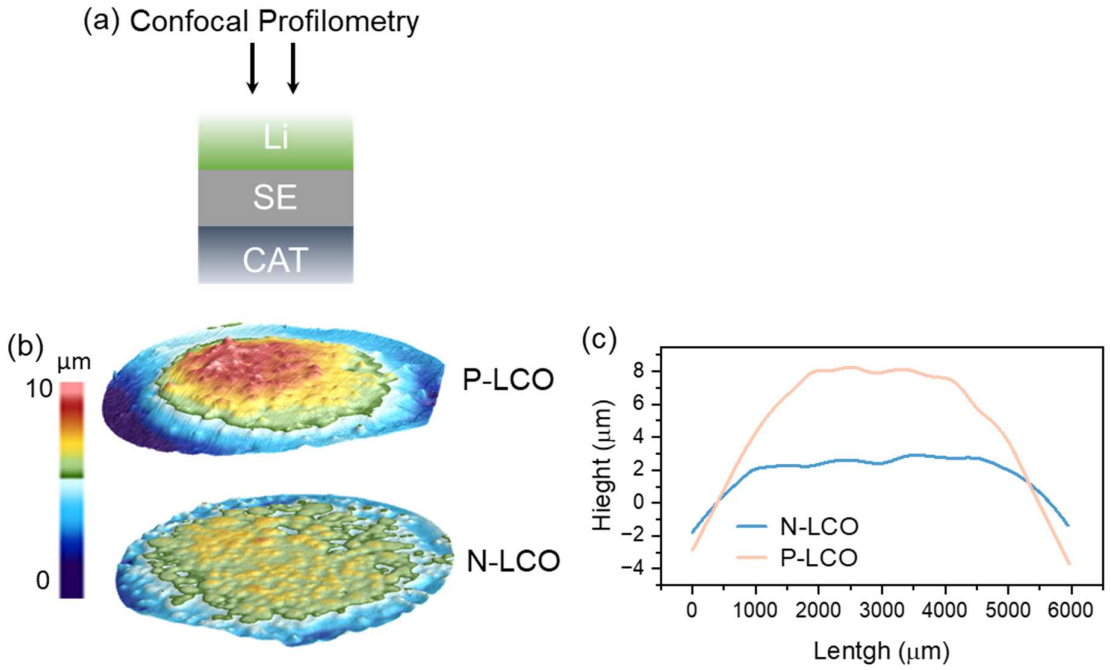

Figure S15 | Confocal profilometry of Li plating/stripping surfaces in P-LCO and N-LCO Li-metal full-cells. (a) Schematic of Li-metal full-cell position against confocal profilometry. (b) 3D surface profile of Li/Cu (current collector) after Li plating and stripping for the P-LCO and N-LCO full-cells at 0.6 mA/cm^2, 1 MPa and 26°C. (c) Hight profile across active region exposed to Li plating/stripping for P-LCO and N-LCO full cells.

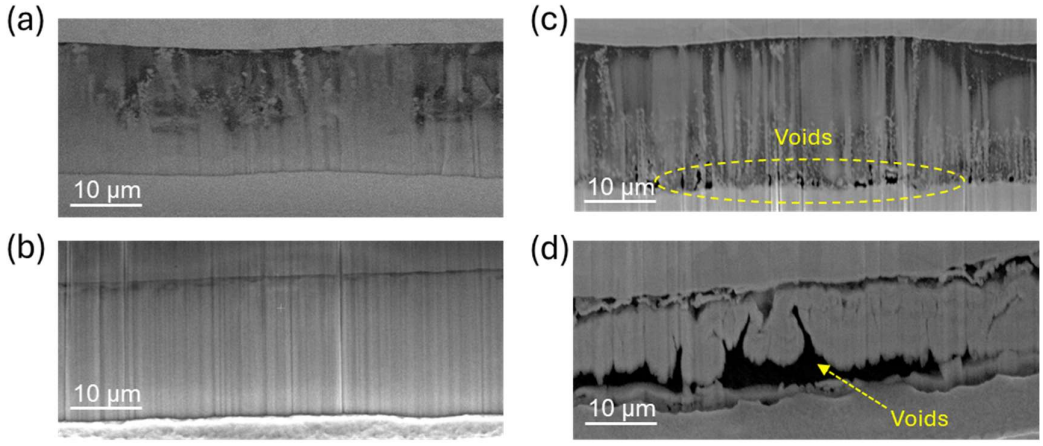

Figure S16 | FIB-SEM analysis of Li-LPSC interfaces with different positive electrodes revealing void formation. (a) N-LCO, showing a void-free Li-SE interface. (b) Composite NMC622 positive electrode, presenting a stable, void-free Li-SE interface. (c) P-LCO, displaying void formation at the Li-SE interface. (d) Composite LCO positive electrode, exhibiting voids at the interface. Images represent typical interfacial morphology under 1 MPa stack pressure, 0.6 mA/cm^2 current density and 26°C, highlighting positive electrode-dependent voiding behavior.

S9. Conventional composite positive electrode Li metal SSBs

Table S2. Solid-state batteries reported in the literature operating at <5 MPa.

Pressure (MPa)	Temp (°C)	Areal Cap. (mAh/cm^2)	Cycle No	Cap. retention	Interlayer	Positive electrode	Ref.
1	60	2.2	350	82.4	LNI–Mg	NMC811	[8]
2	80	3	50	65	N/A	NMC811*	[9]
4	60	6.8	1000	89	Ag-C	NMC91	[10]
2.5	80	7.2	40	80	Mg-Bi	NMC811	[11]
2.5	60	1	100	55	Li_2NH-Mg	NMC622	[12]
2.5	60	2.7	100	70	Li_2NH-Mg	NMC622	[12]
5	55	1.36	2800	75	SiG	NMC83	[13]
1	26	2	500	99	None	NMC622	this study
1	26	5	100	99	None	NMC622	this study
*Li-In alloy is used in this study without an interlayer.							

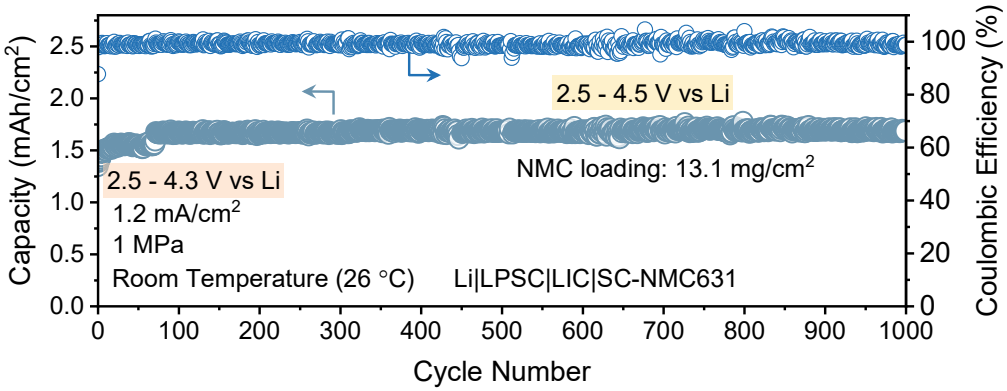

Figure S17 | Long-term cycling of SC-NMC631 electrode without interlayer against Li-metal negative electrode. Long-term cycling performance of single crystalline (SC) NMC631 composite positive electrode cycled at ~1.7 mAh/cm^2 areal capacity in the voltage window of 2.5 – 4.3 V vs Li^+/Li (first 70 cycles) followed by 2.5 – 4.5 V vs Li^+/Li. The cell is cycled under 1 MPa stack pressure at room temperature (26°C) without use of any interlayer at the Li-SE interface. Cell configuration is composite Li|LPSC|LIC|Positive electrode Cycling data shown excludes the initial formation cycle.

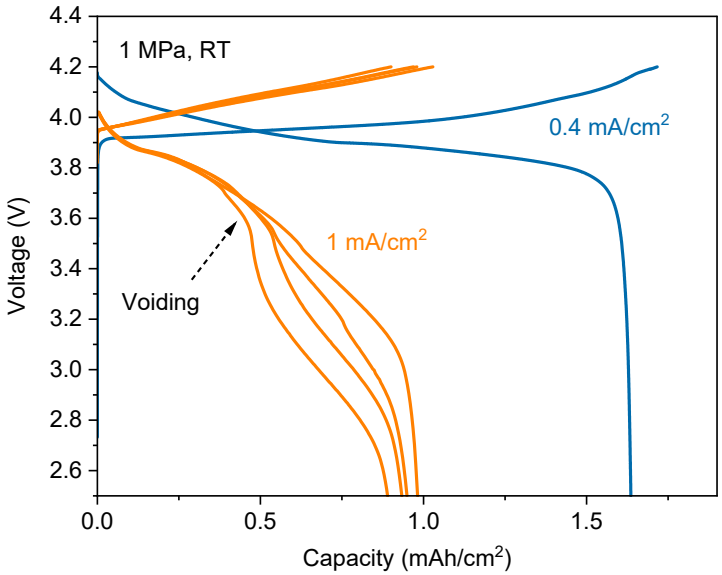

Figure S18 | Cycling behaviour of LCO composite electrode. LCO composite positive electrode (70% LCO, 27% SE, 3% carbon additive) cycled at "safe" (0.4 – 0.5 mA/cm^2) current density in first cycle and then at higher current density (1 mA/cm^2) in consecutive cycles.

S10. Cells fabrication consistency and three-electrode cell design

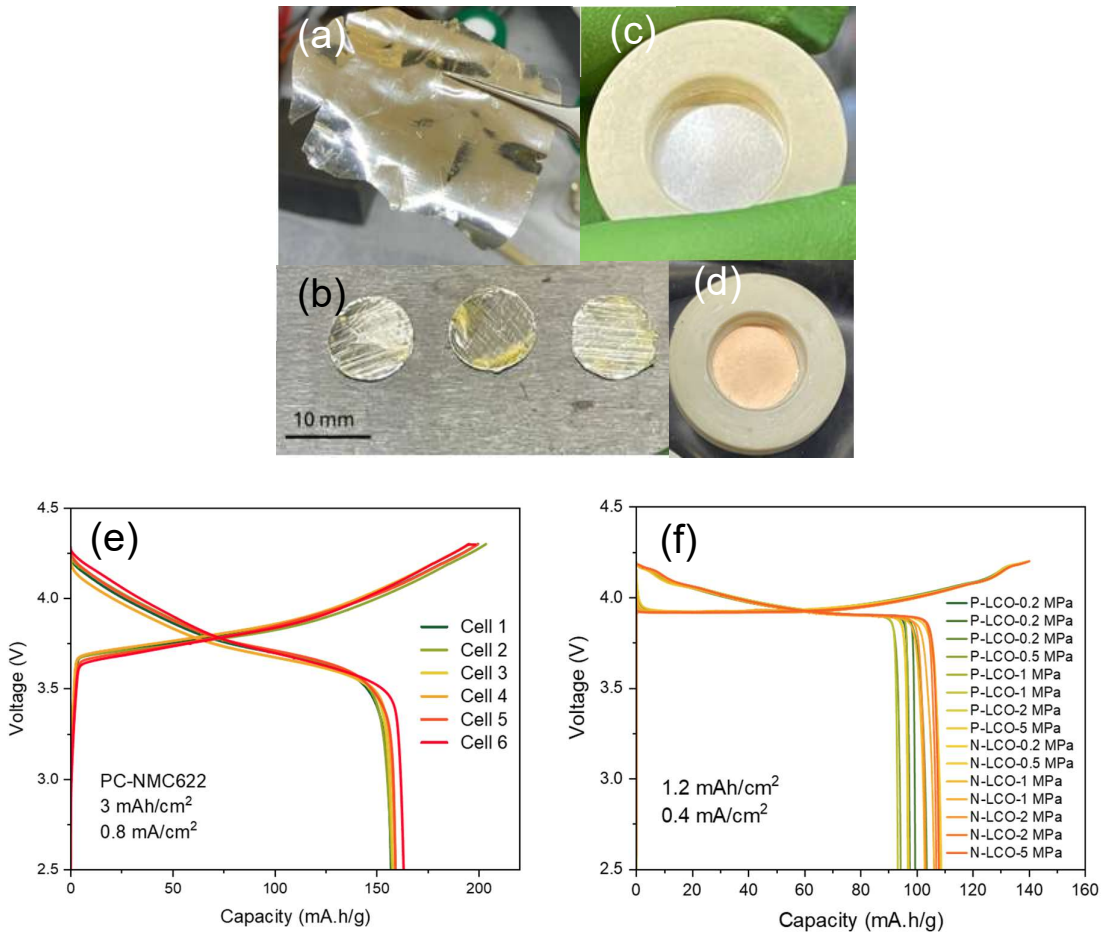

Figure S19 | Reproducible fabrication of thin Li-metal anodes and reliable solid-state cell integration with consistent performance across NMC and LCO positive electrodes. (a) Freshly rolled thin Li metal anode. (b) Punched Li metal pressed onto Cu current collectors. (c) The surface of a densified LPSC SE pallet inside a Ti-die cell without anode. (d) Pressed Li anode onto SE pallet surface. (e) Different PC-NMC622 cells' performance with a cell configuration of Li|LPSC|LIC|NMC at 1 MPa and room temperature. (f) P-LCO and N-LCO cells' performance with a cell configuration of Li|LPSC|LIC|LCO at room temperature.

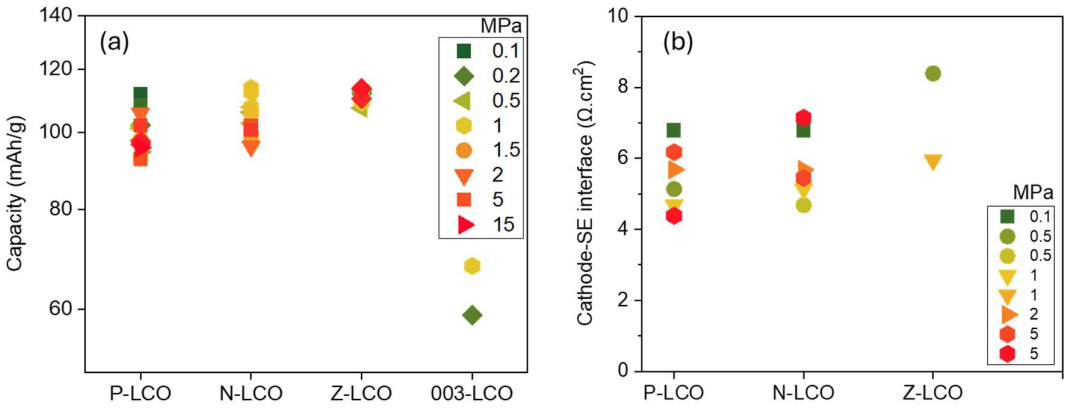

Figure S20 | Impact of stack pressure on LCO performance and electrode–electrolyte interfacial resistance. (a) Discharge capacities achieved for different types of LCO under different stack pressures. (b) Positive electrode/SE interfacial resistance for different positive electrodes at different stack pressures.

A statistical analysis of the performance of various positive electrodes was conducted to examine the role of positive electrode orientation in lithium plating behaviour. Data from multiple assembled cells using N-LCO, P-LCO, and Z-LCO positive electrodes (Figure S20) show no clear correlation between discharge capacity, positive electrode-SE resistance, and the specific positive electrode type used. This absence of correlation indicates that electrochemical performance, in terms of capacity and resistance, does not significantly vary across these LCO positive electrode types. All three positive electrodes, N-LCO, P-LCO, and Z-LCO exhibit nearly identical transport properties, suggesting minimal differences in current density distribution across the positive electrode-solid electrolyte interface that would contribute to uneven lithium plating on the anode side

Further experiments with composite positive electrodes provide additional insight into the observed behaviours. Specifically, the NMC composite positive electrode, which generates negative stress during the charging process (similar to the behaviour observed in N-LCO), does not show any evidence of voiding failure when cycled at a low pressure of 1 MPa and room temperature. In contrast, the composite LCO positive electrode, which generates stress in a manner comparable to P-LCO, is prone to void formation under the same conditions. These observations highlight a critical distinction between the two composite positive electrode materials despite their identical fabrication processes, which ensure consistent positive electrode-SE interfacial adhesion. The fact that composite LCO and NMC positive electrodes, with their differing chemomechanical behavior (such as stress generation during cycling), exhibit these contrasting behaviours underscores the broader applicability of our study's findings. It suggests that the trends observed are not limited to a single material system but are relevant across different positive electrode compositions.

Importantly, in the low SOC region of the positive electrode where voiding is observed in the cell comprised of composite LCO positive electrode (Figure 6 (a) in main text), its electronic and ionic conductivities are higher than those of the NMC composite positive electrode at similar SOC.[14,15,16] This difference implies that the formation of voids in the LCO system is not a result of sluggish positive electrode kinetics, such as limitations in charge transfer or lithium-ion diffusion at the positive electrode/SE interface. Instead, the higher conductivity of LCO during this SOC region suggests that the positive electrode is capable of supporting efficient charge and ion transport, ruling out positive electrode-related kinetic bottlenecks as the primary cause of voiding in this study.

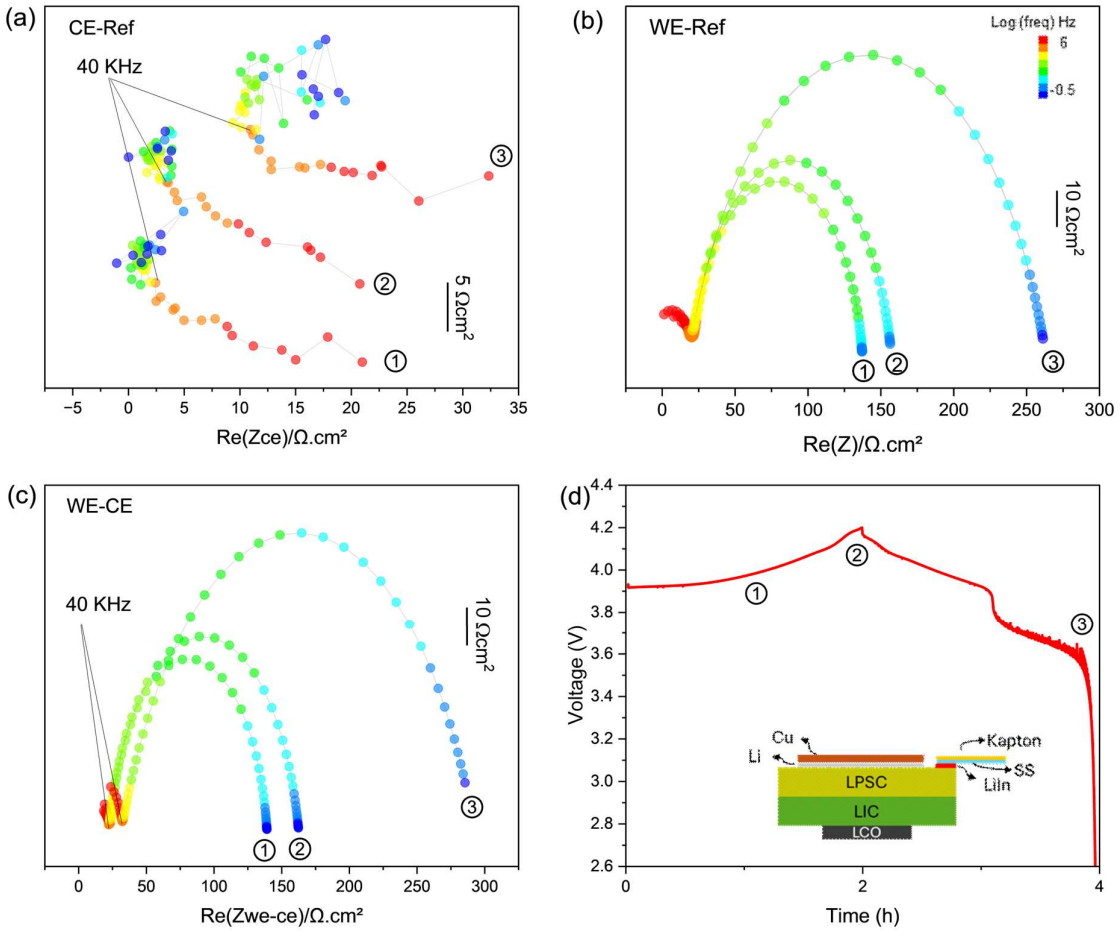

Figure S21 | Impedance analysis of void formation in three-electrode cells under low-pressure cycling. Impedance analysis of a three-electrode cell under 1 MPa stack pressure for interfacial voiding mechanism studies. Nyquist plots depict intra-cycle impedance measurements for: (a) Working Electrode (WE), (b) Counter Electrode (CE), and (c) Overall cell (WE-CE). (d) Corresponding charge/discharge data for P-LCO during void formation alongside with schematic of the three-electrode cell design, illustrating the configuration of WE, CE, and reference electrode (RE).

Fig. S21 provides a clearer picture of the mechanism of void formation under low stack pressure. Based on the analysis of the three-electrode cell EIS data (Fig. S21) and Fig. 4 of the main text, the contributions to the high-frequency impedance variations can be better elucidated. The EIS measurements were conducted at three distinct points during a cycle illustrated in Fig. S21 (d) (1) middle of charge, (2) end of charge, and (3) end of discharge. Fig. S21 (a) shows CE vs. Ref, representing the Li anode impedance; Fig. S21 (b) shows WE vs. Ref, representing the positive electrode impedance; and Fig. S21 (c) shows WE vs. CE, representing the overall cell impedance. The schematic of the three-electrode cell configuration, as shown in Fig. S21 (d), consists of LCO as the positive electrode (WE), LPSC/LIC as double layer SE, and Li metal as the anode (CE). A LiIn alloy reference electrode is integrated within the LPSC electrolyte layer to enable precise potential measurements of the WE and CE separately. The LiIn alloy was chosen as the reference electrode due to its stable electrochemical potential of approximately 0.62 V vs. Li/Li^+, which provides a reliable reference point for measuring the individual potentials of the anode and positive electrode. Additionally, LiIn exhibits good stability in contact with sulfide-based solid electrolytes like LPSC, minimizing

unwanted side reactions, and its relatively low impedance ensures accurate EIS measurements without significant interference.[17]

The EIS data in Fig. S21 (a) (CE vs. Ref), which isolates the Li anode side, reveal that the impedance spectra remain stable throughout the charging process, with no significant shifts. However, at the end of discharge, a shifting towards higher impedance values is observed across the entire frequency range, including the high-frequency region. This shift, as depicted in Fig. S21 (a), is indicative of void formation at the Li/ SE interface. Such voiding likely increases the interfacial resistance, contributing to the observed increase in high-frequency impedance.

In contrast, the EIS data in Fig. S21 (b) (WE vs. Ref), which isolates the positive electrode side, show that the high-frequency region remains relatively stable throughout the cycling process. These panels display consistent high-frequency semicircles with minimal variation, indicating that the positive electrode/SE interface does not undergo significant changes in this frequency range. Instead, variations are primarily observed in the mid-frequency region, which can be attributed to changes in the positive electrode's SOC, as the semicircles shift in a manner consistent with SOC-dependent charge-transfer processes.[18, 19]

Consequently, while the positive electrode contributes to the overall EIS spectra in Fig. S21 (c) (WE vs. CE), its influence is predominantly in the mid-frequency region rather than the high-frequency region. Fig. S21 (c) highlights that the overall high-frequency impedance shift observed at the end of discharge can be primarily attributed to the anode side. The pronounced shift in the high-frequency region of the overall EIS data in Fig. S21 (c) aligns with the changes observed in Fig. S21 (a), reinforcing that the Li/SE interface degradation-specifically void formation-is the dominant factor driving the high-frequency impedance increase.

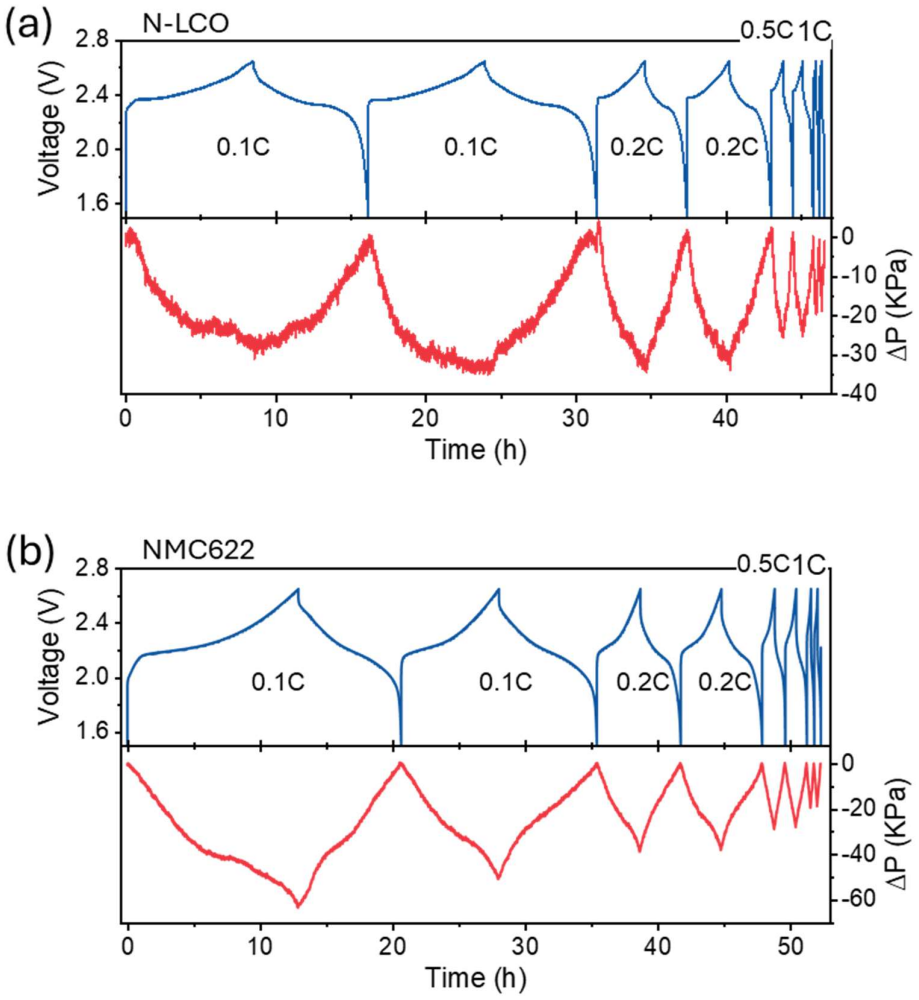

Figure S22 | Axial pressure response of LTO-based cells with N-LCO and NMC622 electrodes under varying cycling rates. Axial pressure monitoring results for (a) N-LCO, (b) NMC622 at cycling rates of 0.1C (0.12 mA/cm^2), 0.2C (0.24 mA/cm^2), 0.5C (0.6 mA/cm^2) and 1C (1.2 mA/cm^2) in cell configuration of LTO|LYC|LIC|LCO and LTO|LYC|LIC|NMC at 26.6°C and 60 MPa respectively. Positive electrodes loading are 1.2 mAh/cm^2.

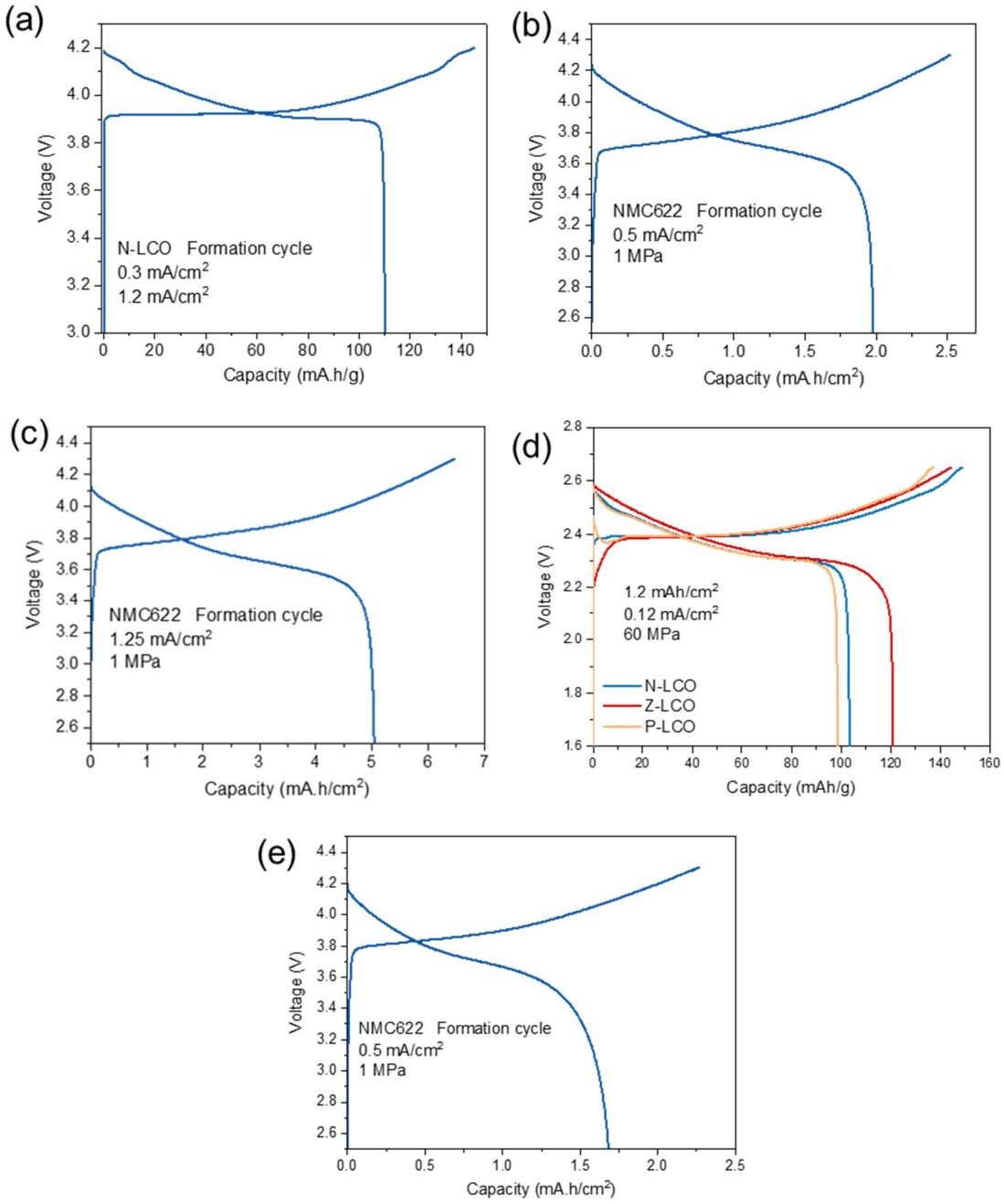

Figure S23 | Formation cycles corresponding to key electrochemical performance figures: Fig. 5(c), Fig. 6(c), Fig. 6(d), Fig. S9, and Fig. S17

Supplementary References

1. Momma, K. & Izumi, F. VESTA: a three-dimensional visualization system for electronic and structural analysis. *urn:issn:0021-8898* **41**, 653–658 (2008).

2. de Biasi, L. *et al.* Between Scylla and Charybdis: Balancing Among Structural Stability and Energy Density of Layered NCM Cathode Materials for Advanced Lithium-Ion Batteries. *J. Phys. Chem. C* **121**, 26163–26171 (2017).

3. Kondrakov, A. O. *et al.* Anisotropic Lattice Strain and Mechanical Degradation of High- and Low-Nickel NCM Cathode Materials for Li-Ion Batteries. *J. Phys. Chem. C* **121**, 3286–3294 (2017).

4. Reimers, J. N. & Dahn, J. R. Electrochemical and In Situ X-Ray Diffraction Studies of Lithium Intercalation in Li x CoO2. *J. Electrochem. Soc.* **139**, 2091–2097 (1992).

5. Koerver, R. *et al.* Chemo-mechanical expansion of lithium electrode materials – on the route to mechanically optimized all-solid-state batteries. *Energy Environ. Sci.* **11**, 2142–2158 (2018).

6. Han, Y. *et al.* Single- or Poly-Crystalline Ni-Rich Layered Cathode, Sulfide or Halide Solid Electrolyte: Which Will be the Winners for All-Solid-State Batteries? *Adv. Energy Mater.* **11**, (2021).

7. Wang, S. *et al.* Lithium Argyrodite as Solid Electrolyte and Cathode Precursor for Solid-State Batteries with Long Cycle Life. *Adv. Energy Mater.* **11**, (2021).

8. Wang, Z. *et al.* Lithium anode interlayer design for all-solid-state lithium-metal batteries. *Nat. Energy* (2024) doi:10.1038/s41560-023-01426-1.

9. Gao, X. *et al.* Solid-state lithium battery cathodes operating at low pressures. *Joule* **6**, 636–646 (2022).

10. Lee, Y.-G. *et al.* High-energy long-cycling all-solid-state lithium metal batteries enabled by silver–carbon composite anodes. doi:10.1038/s41560-020-0575-z.

11. Wan, H., Wang, Z., Zhang, W., He, X. & Wang, C. Interface design for all-solid-state lithium batteries. *Nature* **623**, 739–744 (2023).

12. Wan, H. *et al.* Critical interphase overpotential as a lithium dendrite-suppression criterion for all-solid-state lithium battery design. *Nat. Energy* **8**, 473–481 (2023).

13. Ye, L. *et al.* Fast cycling of lithium metal in solid-state batteries by constriction-susceptible anode materials Check for updates. *Nat. Mater.* | **23**, 244–251 (2024).

14. McClelland, I. *et al.* Direct Observation of Dynamic Lithium Diffusion Behavior in Nickel-Rich, LiNi0.8Mn0.1Co0.1O2 (NMC811) Cathodes Using Operando Muon Spectroscopy. *Chem. Mater.* **35**, 4149–4158 (2023).

15. Lakhdar, Y. *et al.* Toward higher-power Li-ion batteries: Unravelling kinetics and thermodynamics of MoNb12O33 vs. NMC622. *J. Power Sources* **588**, 233710 (2023).

16. Van Der Ven, A. & Ceder, G. Lithium Diffusion in Layered Li x CoO 2. *Electrochem. Solid-State Lett.* **3**, (2000).

17. Chang, G. H., Choi, H. U., Kang, S., Park, J. Y. & Lim, H. T. Characterization of limiting factors of an all-solid-state Li-ion battery using an embedded indium reference electrode. *Ionics (Kiel).* **26**, 1555–1561 (2020).

18. Zahiri, B. *et al.* Revealing the role of the cathode–electrolyte interface on solid-state batteries. *Nat. Mater.* **20**, 1392–1400 (2021).

19. Zhang, W. *et al.* Interfacial Processes and Influence of Composite Cathode Microstructure Controlling the Performance of All-Solid-State Lithium Batteries. *ACS Appl. Mater. Interfaces* **9**, 17835–17845 (2017).